

Simulating Nonadiabatic Dynamics in Benzophenone: Tracing Internal Conversion Through Photoelectron Spectra

Lorenzo Restaino, Thomas Schnappinger, and Markus Kowalewski*

Department of Physics, Stockholm University,

Albanova University Centre, SE-106 91 Stockholm, Sweden

Abstract

Benzophenone serves as a prototype chromophore for studying the photochemistry of aromatic ketones, with applications ranging from biochemistry to organic light-emitting diodes. In particular, its intersystem crossing from the first singlet excited state to triplet states has been extensively studied, but experimental or theoretical studies on the preceding internal conversion within the singlet manifold are very rare. This relaxation mechanism is particularly important because direct population transfer of the first singlet excited state from the ground state is inefficient due to its low oscillator strength. In this work, we aim to fill this gap by employing mixed quantum classical and full quantum dynamics simulations and time-resolved photoelectron spectroscopy for gas-phase benzophenone and *meta*-methyl benzophenone. Our results show that nonadiabatic relaxation via conical intersections leads to a linear increase in the population of the first singlet excited state. This population transfer due to conical intersections can be directly detected by a bifurcation of the photoelectron signal. In addition, we are able to clarify the role of the third singlet excited state degenerate to the second excited state — a topic that remains largely unexplored in the existing literature on benzophenone.

* e-mail: markus.kowalewski@fysik.su.se

I. INTRODUCTION

Benzophenone (BP) is an organic chromophore frequently employed as a prototype for investigating the photochemistry of more complex aromatic ketones. This type of chromophore has a rich photochemistry under ultraviolet (UV) light, which involves several nonadiabatic steps: a conical intersection (CoIn) between the first two singlet excited states, S_2 and S_1 , and subsequent efficient intersystem crossing processes between the S_1 and several triplet states. Especially due to the latter BP and many of its derivatives have significant applications in technological and biological contexts, including organic light-emitting diodes [1, 2], UV filters [3, 4], and photosensitizers [5, 6]. The existing literature on the photochemistry of BP is extensive, but most experimental and theoretical studies [7–12] focus on the mechanisms leading to direct and indirect population of the lowest triplet excited state, T_1 , starting from S_1 [11]. However, the S_1 state has a negligible cross-section and cannot be efficiently populated directly from the ground state. The experimental more realistic pathway is to excite the system to higher lying singlet states of $\pi\pi^*$ character, which have a stronger oscillator strength, and populate S_1 via internal conversion.

The S_2/S_1 CoIn has been the subject of two experimental investigations by Shah et al. [13] and Spighi et al. [8]. In their study, Shah et al. employed time-resolved absorption spectroscopy with a full width at half maximum (FWHM) ≈ 150 fs pump pulse centered at 267 nm (≈ 4.66 eV). They measured a lifetime of 0.53 ps for the S_2 state in acetonitrile following the growth in absorption of the S_1 state, and a kinetic rate of $1.7 - 1.9 \cdot 10^{12} \text{ s}^{-1}$ for the $S_2 \rightarrow S_1$ internal conversion. Spighi et al. investigated the excited state dynamics of gas-phase BP via femtosecond and nanosecond resonance-enhanced multiphoton ionization, employing a pump pulse centered at 266 nm (≈ 4.66 eV), with a pump-probe cross-

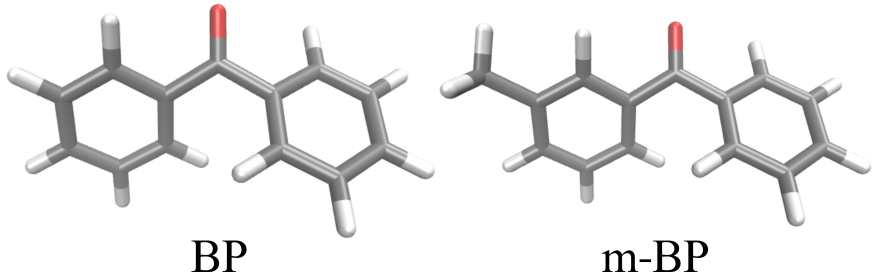


Figure 1. Molecular structures of benzophenone and *meta*-methyl benzophenone.

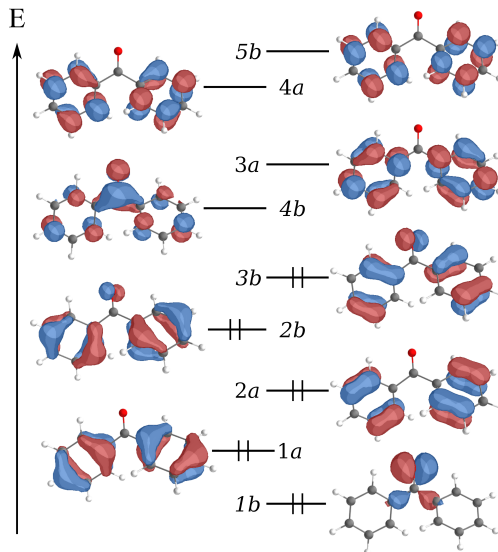


Figure 2. Valence molecular orbital diagram of ground-state BP at the CAS(16,15)/ANO-L-VDPZ level of theory. The molecular orbitals are labeled according to C_2 symmetry. The numbering for the oxygen lone pair in the diagram is arbitrarily set to 1. An isovalue of 0.05 was used to generate the molecular orbital plots.

correlation of approximately 100 fs. The authors observed an exponential rise and decay of photoelectron bands with a time constant of 150 fs, which they attributed to internal conversion to S_1 . However, as the authors stated, the multiphoton ionization probe made it impossible to unambiguously assign each band in the photoelectron spectra to a single electronic state. The resonance-enhanced multiphoton ionization scheme involves several intermediate states providing multiple pathways and resonance conditions, further complicating the interpretation.

Both experiments provide evidence of the ultrafast nonradiative decay from the S_2 state, indicating the presence of a conical intersection between S_2 and S_1 . However, the temporal resolution of the two experiments cannot resolve the intricate ultrafast excited-state dynamics occurring within the first 100 fs. Moreover, the existence of the S_3 state, which is almost degenerate to the S_2 state, has not been taken into account in the interpretation of the experimental results. The S_1 state has $n\pi^*$ character and belongs to the irreducible representation A under C_2 symmetry. The $S_0 \rightarrow S_1$ transition predominantly involves the promotion of an electron from the oxygen lone pair, $1b$, to the lowest unoccupied molecular orbital (LUMO), $4b$ (see fig. 2). Both S_2 and S_3 have $\pi\pi^*$ character and belong to the irre-

ducible representations A and B , respectively. The $S_0 \rightarrow S_2$ transition primarily involves π electron excitations from $2b$ to $3b$ and from $2a$ to $3a$; while the $S_0 \rightarrow S_3$ transition involves π excitations from $1a$ to $4b$ and from $2b$ to $4a$. Given that the energy difference between S_2 and S_3 is predicted on the order of 10^{-2} eV, the experimental pump pulse resolution cannot differentiate them. Consequently, both states can be expected to be populated under experimental conditions [8, 13], adding another piece to the puzzle. In this work we determine time-resolved photoelectron spectra based on the excited state dynamics in the singlet manifold of the gas phase BP and its methylated derivative *meta*-methyl benzophenone (m-BP), displayed in fig. 1, to show that (i) the rise in the population of the S_1 state is linear, and it is accompanied by a similar linear increase in the corresponding photoelectron band. Beyond that, the internal conversion can be associated with a bifurcation of the photoelectron signal; (ii) the inclusion of the S_3 state reveals ultrafast population transfer to S_2 , due to the presence of a conical intersection in the vicinity of the Franck-Condon (FC) point.

II. COMPUTATIONAL DETAILS

All calculations were performed in a reproducible environment using the Nix package manager together with NixOS-QChem [14] (commit 9b40085ca).

A. *Ab initio* level of theory

All calculations were performed in gas phase, in C_1 symmetry. Geometry optimizations and frequency analysis were carried out at the ω B97X-D2 [15, 16]/6-311G(d) [17] level of theory using the Gaussian 16 RevC.01 [18] quantum chemistry program. The excited states of BP and m-BP were determined by linear response density functional theory (LR-DFT), complete active space self-consistent field (CASSCF) as well as density functional theory / multi-reference configuration interaction (DFT/MRCI) theories. The LR-DFT calculations were carried out within the Tamm-Dancoff approximation (TDA) [19] using ω B97X-D4 [20]/6-311G(d) level of theory in the ORCA 5.0.4 program package [21, 22]. The state-average SA-CASSCF calculations were performed using OpenMolcas v.24.02 [23, 24], with the ANO-L-VDZP [25] basis set, averaging over 4 states. After the CASSCF calculation, dynamic electron correlation was added using extended multi-state complete

active space 2nd order perturbation theory (XMS-CASPT2) [26, 27].

The configuration interaction (CI) expansion for CASSCF scales nearly exponentially with the number of active orbitals and electrons. The full π -system of BP requires an active space of 16 electrons in 15 orbitals. The full CAS(16,15) active space is shown in the supporting information fig. S1. This computation is quite time-consuming, and complete active space 2nd order perturbation theory (CASPT2) becomes impractical for the purpose of calculating excited state dynamics. Although this active space can still be used to benchmark some critical points, it is not suitable for constructing global potential energy surfaces. For this reason, we employed a DFT/MRCI approach to achieve balance between computational costs and accuracy.

Two-dimensional potential energy surfaces, diabatic couplings and transition dipole moments (TDMs) of the ground state and three singlet excited states of m-BP were calculated at the DFT/MRCI(2) [28–30] level using the QTP17 [31] xc-functional, the QE8 hamiltonian [30] and the 6-311G(d) basis set. The quasi-diabatic states and potentials were obtained by a procedure using quasi-degenerate perturbation theory [32] as implemented in GRACI [33]. The active space used in the DFT/MRCI calculations is shown in figs. S3 and S4 of the supporting information (SI). The raw values (energies, couplings, and transition dipole moments) were then interpolated with polyharmonic splines [34] onto a fine grid ($N_1 = N_2 = 128$ points), for the wave packet dynamics.

B. Surface Hopping Dynamics

The molecular dynamics of BP and m-BP were simulated using the SHARC *ab initio* dynamics package version 3.0 [35, 36]. The necessary energies, gradients and non-adiabatic couplings were calculated on-the-fly at the TDA/ ω B97X-D4/6-311G(d) level of theory. In total, 1000 initial conditions for the dynamics simulations were generated based on a Wigner distribution computed from harmonic vibrational frequencies in the optimized ground state equilibrium geometry. The underlying frequency calculations were performed at ω B97X-D2/6-311G(d) level of theory. Altogether, 160 initial geometries and velocities, 68 in state S_2 and 92 in state S_3 were chosen stochastically.

The SHARC *ab initio* surface-hopping algorithm uses a fully diagonal electronic basis [37, 38]. The integration of the nuclear motion was done with the Velocity-Verlet algo-

rithm with a maximal time of 0.5 ps using a time step of 0.5 fs. In each time step, gradients were computed for all states which are closer than 0.001 eV to the active state. The coefficients of the electronic wave function are propagated on interpolated intermediates with a time step of 0.02 fs applying a local diabaticization technique [39] in combination with the WFOverlap code [40] to compute the wave function overlaps. Decoherence correction was taken into account using the energy-based method of Granucci and Persico with the parameter $\alpha = 0.1$ a.u. [41] We restricted our analysis to trajectories with a maximum change in the total energy of 0.3 eV and a maximum change in the total energy per step of 0.2 eV. All trajectories are included in the analysis as long as both criteria are fulfilled. At 500 fs, 55% of the trajectories for BP and 50% of the trajectories for m-BP met the energy conservation criteria.

For each geometry, Dyson norms were calculated between 4 neutral and 4 cationic states through the WFOverlap code [40, 42] at the TDA/ ω B97X-D4/6-311G(d) level of theory. Excitation energies and corresponding Dyson norms were employed to generate a photoelectron spectrum, which was then broadened by a Gaussian function with a full width at half maximum of 0.4 eV.

C. Quantum Dynamics Simulations

The wave packet dynamics of the photoexcited m-BP was calculated by solving the time-dependent (non-relativistic) Schrödinger equation numerically with the Fourier method [43–45], using the in-house software package QDng [46]. To propagate the wave packet on the potential energy surfaces, we used a Hamiltonian in a diabatic basis and coordinates q :

$$\hat{H} = \begin{pmatrix} \hat{T} + \hat{V}_{S_0}(q) & 0 & 0 & 0 \\ 0 & \hat{T} + \hat{V}_{S_1}(q) & \hat{V}_{S_1S_2}(q) & 0 \\ 0 & \hat{V}_{S_1S_2}(q) & \hat{T} + \hat{V}_{S_2}(q) & \hat{V}_{S_2S_3}(q) \\ 0 & 0 & \hat{V}_{S_2S_3}(q) & \hat{T} + \hat{V}_{S_3}(q) \end{pmatrix}, \quad (1)$$

where \hat{T} is the kinetic energy operator, \hat{V}_{S_0} , \hat{V}_{S_1} , \hat{V}_{S_2} and \hat{V}_{S_3} are the diabatic potentials for the states S_0 , S_1 , S_2 and S_3 , respectively. The diabatic couplings are given by $\hat{V}_{S_1S_2}$ and $\hat{V}_{S_2S_3}$. The kinetic operator is in the G-matrix form [47]:

$$\hat{T} = -\frac{\hbar^2}{2} \sum_{r=1}^M \sum_{s=1}^M \left[G^{rs} \frac{\partial^2}{\partial q_r \partial q_s} \right], \quad (2)$$

where M is the number of coordinates taken into considerations. The expression in (2) derives from the assumption that the elements of the Wilson G-matrix are constant. The term G^{rs} indicate the element of kinetic energy matrix equal to:

$$G^{rs} = \sum_{i=1}^{3N} \frac{1}{m_i} \frac{\partial q_r}{\partial x_i} \frac{\partial q_s}{\partial x_i}. \quad (3)$$

Here N is the total number of atoms and m_i the mass of atom i . In eq. (3), diagonal entries are reciprocals of generalized reduced masses, and the off-diagonal entry is the kinetic coupling term. The calculated values are given here in atomic units: $G_{rr} = 0.0001447$, $G_{ss} = 0.00016924$ and $G_{rs} = -5.101169 \cdot 10^{-6} \text{ au}^{-1}$. The short iterative Lanczos scheme [48–50] was used to propagate the nuclear wave packet and the Hamiltonian form eq. 1 with a time step of $\Delta t = 1 \text{ au}$ (24.2 as). The total wave function was expressed as a linear combination

$$\Psi = \sum_{i=0}^4 c_i \phi_i \quad (4)$$

with $c_0 = c_1 = 0$, $c_2 = \sqrt{0.4}$ and $c_3 = \sqrt{0.6}$. These values were specifically chosen to replicate the initial populations of the surface hopping dynamics.

III. RESULTS AND DISCUSSION

A. Benchmark of Vertical Excitations

Before we introduce the molecular dynamics and the simulated time-resolved photoelectron spectra for BP and m-BP, we discuss the vertical UV excitations and ionization energies of the two molecules. Table I provides a benchmark of calculated vertical excitations for BP against the experimental values taken from reference [51]. This includes the level of theory used in surface hopping dynamics (TDA), the level of theory used to construct potential energy surfaces (PESs) (DFT/MRCI), and the multireference method (CASPT2) that employs the full π system of BP (CAS(16,15) with 4-state averaging). An even more extensive benchmark, including CASPT2 with different sizes of the active space and RASPT2 calculations, can be found in the SI in tables S1 to S4. Additional computational details are given in the table caption and in section II. As expected, the CASPT2 calculations predict vertical excitations very close to the experimental values and are therefore well suited

Table I. Comparison between vertical excitation energies and their corresponding oscillator strength of BP, calculated at TDA/ ω B97x-D4/6-311G*, DFT/MRCI(2)/QTP17/QE8/6-311G* and XMS-CASPT2/CAS(16,15)/ANO-L-VDPZ levels of theory.

	Energies (eV)				Oscillator Strength		
	TDA	DFT/MRCI	CASPT2	Exp	TDA	DFT/MRCI	CASPT2
S_1	4.04	4.04	3.65	3.61 ^a	0.0010	0.0040	0.0007
S_2	5.36	4.94	4.60	4.40 ^a	0.015	0.0213	0.0036
S_3	5.40	4.98	4.62	4.40 ^a	0.015	0.0114	0.0023

^a low pressure vapor, ref. [51]

as a general criterion for validating the other theoretical methods applied. In contrast, DFT/MRCI and especially TDA calculations generally overestimate the excitation energies. The DFT/MRCI results are slightly more accurate, but still produce vertical transitions that are systematically blueshifted by approximately 0.4 eV. Meanwhile, TDA calculations tend to overestimate $\pi\pi^*$ transitions by nearly 1 eV. Nonetheless, all methods capture the near degeneracy between S_2 and S_3 . Both DFT/MRCI and TDA predict an energy difference between S_3 and S_2 of 0.04 eV. According to CASPT2 calculations, the energy difference between S_2 and S_1 at the FC point is 0.95 eV, which is slightly above the experimental value of 0.79 eV. Likely due to error compensation, the DFT/MRCI method predicts a 0.9 eV gap, performing better than CASPT2. The TDA calculations yield the largest energy gap at 1.32 eV. This overestimation of the S_2/S_1 energy gap may result in a slower population transfer in the surface hopping dynamics. All methods consistently predict the right trend for the oscillator strengths, identifying $S_0 \rightarrow S_1$ as the weakest transition.

Table II shows the vertical excitation energies calculated for m-BP. Although we were unable to find any experimental UV spectrum data for gas-phase m-BP to directly compare with our calculations, we anticipate that it will not differ significantly from that of the parent molecule. TDA and DFT/MRCI calculations yield the same value for the $S_0 \rightarrow S_1$ transition as observed for BP, suggesting that the methyl group in *meta* has negligible influence of on the CO π bond. The predicted energy gap between S_3 and S_2 is 0.14 eV with TDA and 0.12 eV with DFT/MRCI, where the splitting arises mainly from a stabilization effect on the S_2 state. The energy gap between S_2 and S_1 at the FC is calculated to be smaller for

Table II. Comparison between vertical excitation energies and their corresponding oscillator strength of m-BP, calculated at TDA/ ω B97x-D4/6-311G* and DFT/MRCI(2)/QTP17/QE8/6-311G* levels of theory.

	Energies (eV)		Oscillator Strength	
	TDA	DFT/MRCI	TDA	DFT/MRCI
S_1	4.04	4.00	0.0010	0.0023
S_2	5.25	4.80	0.0220	0.0279
S_3	5.39	4.92	0.0133	0.0124

m-BP than BP. DFT/MRCI calculations place it at 0.8 eV, whereas TDA estimates it at 1.21 eV. Similarly to BP, the overestimation of the energy difference between S_2 and S_1 may slow down the population transfer during the surface hopping dynamics. The energies calculated over a Wigner distribution (see section II for more details) have been convoluted with a Gaussian (FWHM = 0.4 eV) to produce the UV spectra of BP and m-BP, as shown in fig. 3 (a) and (b), respectively. Consistent with the findings at the FC point presented in tables I and II, the optically brighter region of the TDA spectrum shows a blue shift of 0.4 eV compared to DFT/MRCI. There are no notable distinctions between BP and m-BP.

The ionization spectrum of gas-phase BP has been the subject of several experimental and theoretical studies [52–55]. The experimental spectrum measured by Centineo et al. [52] shows an overlapping band in the 8-10 eV range with two distinguishable peaks at approximately 9.0 and 9.45 eV, along with two shoulders at higher energies. The calculated static photoelectron spectrum of BP is shown in fig. 4. The CASPT2 calculations including the complete π system of BP are in good agreement with the experiment. The lack of a shoulder at higher binding energies is due to the absence of the corresponding electronic states in the SA-CASSCF calculations, which averaged over four states of the cation. The photoelectron spectrum calculated with TDA accurately models the D_0 state, but it overestimates the ionization energies for D_1 , D_2 , and D_3 , which are blueshifted by approximately 0.5 eV.

Overall, although there are some quantitative differences, we are convinced that TDA and the chosen functional are adequate to describe the mixed quantum classical dynamics of BP and m-BP.

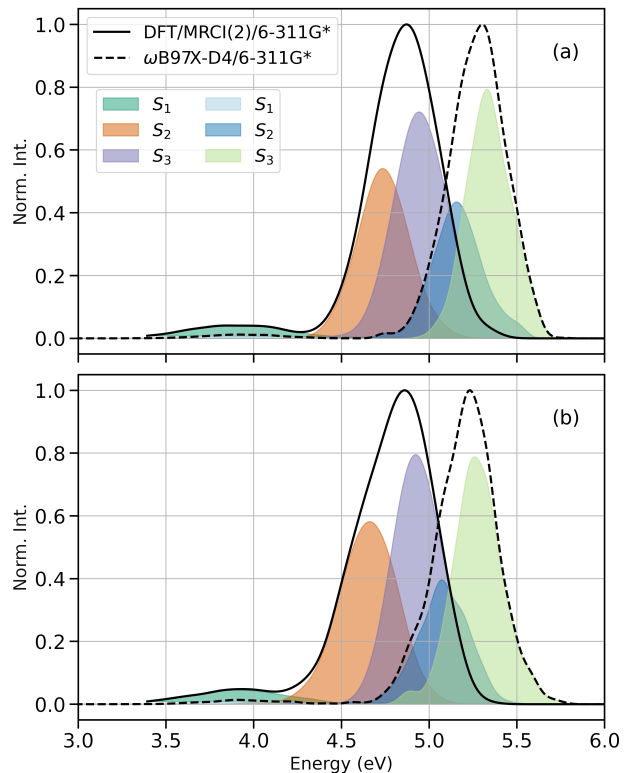


Figure 3. Unshifted UV spectra of benzophenone (a) and *meta*-methyl benzophenone (b) calculated over their respective Wigner distributions with TDA (dashed line) and DFT/MRCI (solid line).

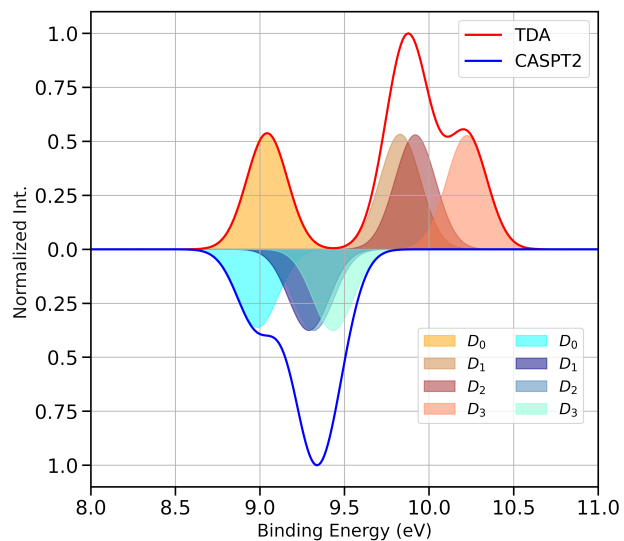


Figure 4. Static photoelectron spectrum of ground-state BP calculated with TDA/ ω B97X-D4 (red color scheme) and XMS-CASPT2 (blue color scheme). To prevent overlapping features, the CASPT2 spectrum is shown up-side-down.

B. Semiclassical Dynamics and Time-resolved Photoelectron Spectra

Having validated the *ab initio* method, we will now discuss the excited-state dynamics of BP and m-BP, starting with the parent molecule. Note that the number of trajectories satisfying the total energy conservation criteria decreases with time. This time-dependent number of trajectories was used to construct the photoelectron spectra and the populations of the singlet manifold. The on-the-fly selection criteria are discussed in section II. Upon excitation to the S_2 or S_3 state, for all analyzed trajectories nonadiabatic processes are observed.

The time evolution of the average adiabatic populations along the BP trajectories is shown in the top panel of fig. 5. The second y-axis represents the fraction of trajectories (gray line) that satisfy the total energy conservation criteria at each time step. The trajectories reveal a rapid exponential decay of the S_3 population to S_2 within the initial 10 fs of the dynamics, and the nonadiabatic relaxation is completed within 50 fs. The strong depletion in the S_3 population suggests that S_3 and S_2 are strongly coupled and that there is a favorable gradient towards S_2 . After 40 fs, an almost linear increase in the S_1 population can be observed, along with a corresponding decrease in the S_2 population. As more population goes into S_1 of $n\pi^*$ anti-bonding character, an elongation of the CO bond can be observed, as shown in fig. S6 of the SI. The normal modes analysis of the SHARC trajectories within the first 150 fs reveals that the dihedral movement between the two aryl rings is predominant. Nevertheless, a direct correlation between the dihedral oscillations and the photoelectron observable could not be established. The normal mode analysis is available in the SI in fig. S5.

The lower left panel of fig. 5 displays a snapshot of the time-resolved photoelectron spectrum taken at time zero. The dashed lines indicate the binding energies at the FC point, with the same color scheme as the population plot in fig. 5. The snapshot spectrum consists of two bands, approximately centered at 3.6 and 4.7 eV. With the temporal evolution of the populations in mind, we are now able to discuss the time-resolved photoelectron spectrum of BP, shown in the lower right panel of fig. 5. Note that due to the different characteristic of the probe (multiphoton vs single photon ionization), we cannot directly compare our results to the experiment of Spighi et al. [8]. During the initial 15 fs of the dynamics, a distinct blueshift of the two bands is observed in the time-resolved photoelectron spectrum, along

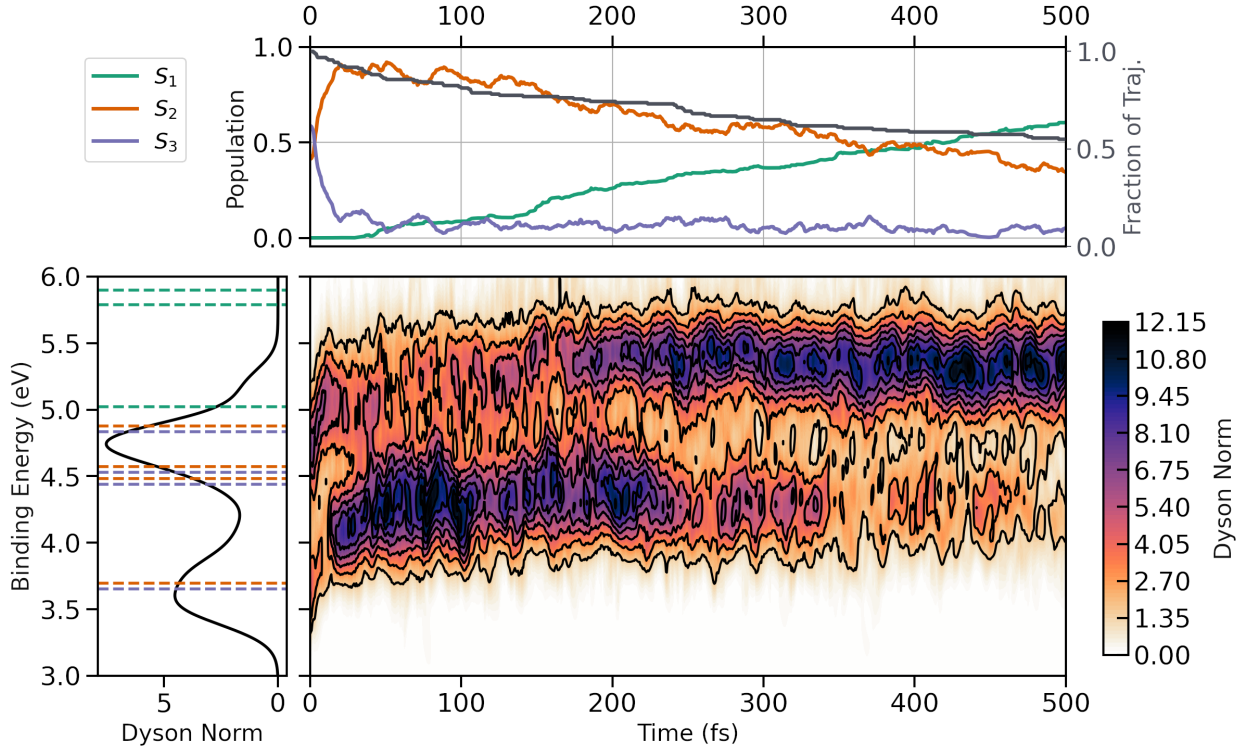


Figure 5. Time-resolved photoelectron spectrum of BP computed at the TDA/ ω B97X-D4/6-311G* level of theory from the combined trajectories of S_2 and S_3 . Upper panel: time evolution of the average adiabatic populations along the BP trajectories. The second y-axis shows the fraction of trajectories (grey line) meeting the total energy conservation criteria at each time step, used for calculating the spectrum and time-dependent populations of the singlet manifold. A unitary fraction corresponds to 160 trajectories, with a minimum fraction of ≈ 0.55 equivalent to 88 trajectories. Lower left panel: temporal slice of the time-resolved photoelectron spectrum selected at 0 fs. Dashed lines indicate binding energies at the Frank-Condon point, using the color scheme of the population plot. Lower right panel: full time-resolved photoelectron spectrum.

with a notable inversion in intensity. The band originating at 3.6 eV experiences a blueshift of approximately 0.4 eV and an increase in intensity, while the band at 4.7 eV experiences a blueshift of approximately 0.3 eV and a decrease in intensity. The internal conversion from S_3 to S_2 is responsible for this feature of the time-resolved photoelectron spectrum. The observed intensity exchange matches the exponential decay of the S_3 population. Moreover, the blueshift suggests a favorable gradient towards S_2 . After 50 fs, the bifurcation of the band centered at 3.6 eV becomes increasingly more evident. The signal covers a broad spectral

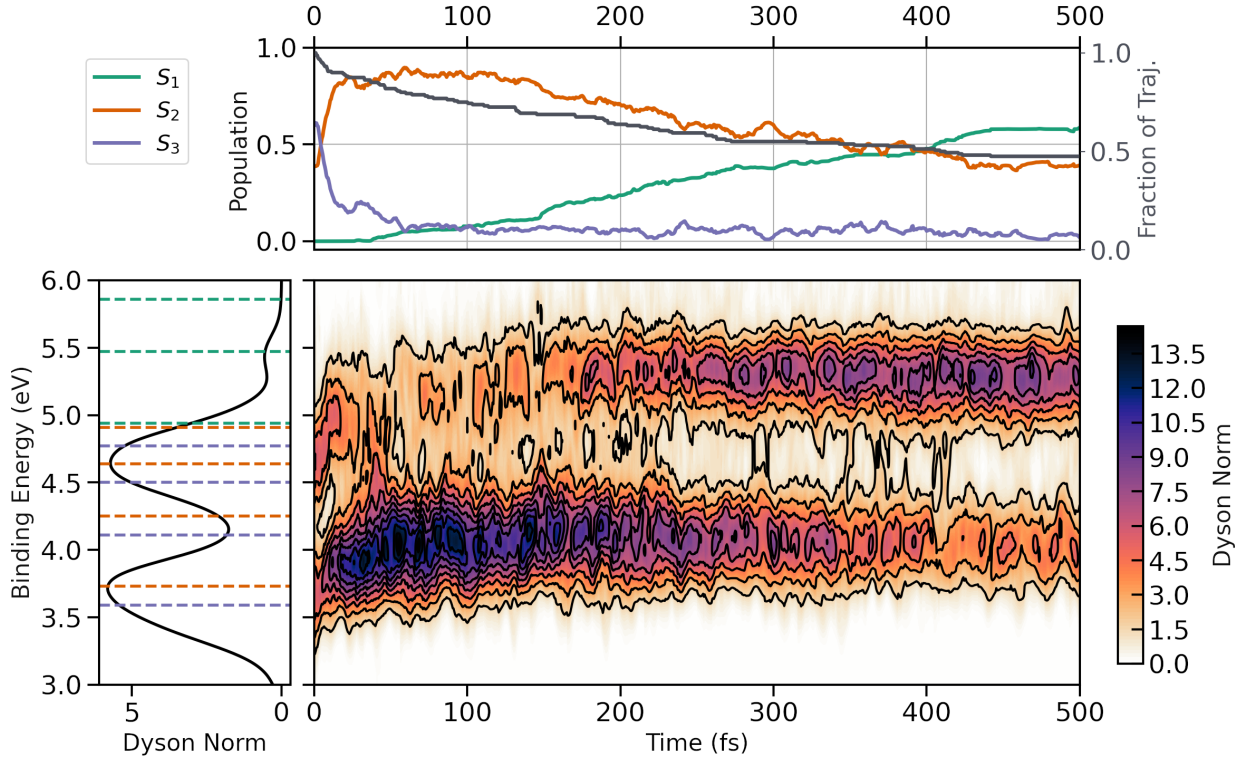


Figure 6. Time-resolved photoelectron spectrum of m-BP computed at the TDA/ ω B97X-D4/6-311G* level of theory from the combined trajectories of S_2 and S_3 . Upper panel: time evolution of the average adiabatic populations along the m-BP trajectories. The secondary y-axis shows the fraction of trajectories (grey line) meeting the total energy conservation criteria at each time step. A unitary fraction corresponds to 160 trajectories, with a minimum fraction of ≈ 0.5 equivalent to 76 trajectories. Lower left panel: temporal slice of the time-resolved photoelectron spectrum selected at 0 fs. Dashed lines indicate binding energies at the FC point, maintaining the color scheme of the population plot. Lower right panel: full time-resolved photoelectron spectrum.

range, from 4 to 5.5 eV. Ultimately, two distinct bands can be identified after 190 fs. As will be shown later, this spectral feature is even more pronounced in the case of m-BP. In addition to the splitting of the signal, a distinctive change in intensity is also observed. In particular, the intensity of the new band emerging at 5.3 eV increases linearly, while the other decreases steadily. The nearly linear increase in the intensity profile of the new band is consistent with the time-dependent evolution of the S_1 population and its timescale. Therefore, we attribute the bifurcation in the photoelectron signal to the population transfer from S_2 to S_1 .

The top panel of fig. 6 shows the time evolution of the average adiabatic populations along the m-BP trajectories. Although the observed features in the population dynamics are very similar to the parent molecule, some small differences also emerge. The depletion of the S_3 population remains exponential. However, a comparison between the two molecules reveals that, during the first 60 fs, the population transferred from S_3 to S_2 is about 10% greater in BP than in m-BP. After this initial phase, the populations in S_3 for both molecules become approximately the same. These features can be better appreciated in fig. S9 of the SI. These differences can be attributed to a larger energy gap between S_3 and S_2 , resulting in weaker coupling of the states in m-BP. After a simulation time of 500 fs, 60% of the total population reside in S_1 for both molecules, we conclude that the presence of a methyl group in *meta* position does not significantly affect internal conversion from S_2 to S_1 . Similarly to the parent molecule, there is a direct correlation between the increase in population of S_1 and the elongation of the CO bond (fig. S6 in the SI).

The spectral snapshot of the time-resolved photoelectron spectrum at 0.0 fs, shown in the left panel of fig. 6, displays an intensity profile different from that of BP. In particular, the bands centered at 3.6 and 4.7 eV now show an equal intensity. The time-resolved photoelectron spectrum of m-BP is displayed in fig. 6. As in the BP situation, the m-BP spectrum exhibits a blueshift of ≈ 0.4 eV of these two bands during the initial 15 fs of dynamics, paired with an exponential change in their intensity. Following this, the signal at 3.9 eV splits, resulting in a linear rise in the intensity of the S_1 signal, while the intensity of the S_2 signal decreases. Similarly to the parent molecule, the blueshift, accompanied by the exponential decay/rise in the intensity profile, mirrors the nonadiabatic relaxation from S_3 to S_2 . The signal bifurcation and the linear increase in intensity of the newly emerged band correspond to the nonadiabatic relaxation from S_2 to S_1 , and they appear more pronounced here than BP. There is no clear connection between the dihedral oscillations of the aryl rings and the photoelectron spectrum.

C. Construction of Potential Energy Surfaces

The construction of diabatic PESs for BP was unattainable due to numerical problems in the diabatization process, attributed to the degeneracy of S_2 and S_3 , and the resulting coupling already at the FC point. To address this issue, we opted for a methylated ben-

zophenone as a candidate to construct diabatic PESs and carry out subsequent quantum dynamics (QD) simulations. Indeed, despite the presence of a methyl group, the photochemistry of m-BP does not change significantly, making the two systems quite comparable, as demonstrated by the UV spectrum based on a Wigner sampling in fig. 3. Positioning the methyl group in *meta* yields a sufficiently large splitting between the S_3 and S_2 states enough to reduce their coupling at the FC point, without introducing a strong steric effect on the relaxation dynamics. This, in turn, facilitates the construction of diabatic PESs. Moreover, asymmetric substitution of the aryl rings breaks the C_2 symmetry of BP.

The number of vibrational degrees of freedom (d.o.f.) for m-BP is $3N - 6 = 75$, where N is the number of atoms in the molecule. In grid-based methods, the size of the nuclear wave function increases exponentially with the number of nuclear d.o.f., which makes the task computationally prohibitive to solve unless we restrict ourselves to the reactive subspace of the multidimensional problem. In such cases, a choice of reaction coordinate space is required. To describe the initial dynamics associated with the transfer of population from S_2 to S_1 , the difference vector between the FC and CoIn geometries was selected as the primary coordinate:

$$\mathbf{v}_1 = \mathbf{R}^{\text{FC}} - \mathbf{R}^{\text{CoIn}}. \quad (5)$$

This ensures the presence of the S_2/S_1 CoIn in the coordinate space by construction. The primary motion of this coordinate qualitatively describes a ring-puckering vibration. The analysis of the BP and m-BP SHARC trajectories revealed that, within the first 150 fs, the dominant motion involved the dihedral angle between the two aryl rings. The normal mode analysis is available in the SI in fig. S5. For this reason, the vector describing this motion was chosen as the second coordinate (\mathbf{v}_2). The two vectors appointed as reaction coordinates are depicted in SI in fig. S7.

After removing the purely translational and rotational components from the two vectors by satisfying the Eckart conditions [56, 57], we orthonormalized the two coordinates using Löwdin’s orthogonalization scheme. We then calculated a 2D rectangular grid by scanning the two vectors using the FC point as reference geometry:

$$\mathbf{R}_{xyz}^{\text{new}} = \mathbf{R}_{ref} + q_1 \mathbf{v}_1 + q_2 \mathbf{v}_2 \quad (6)$$

with coefficients q_1/q_2 in the range $[-3, 3]$. We conducted an unrelaxed scan of the reaction coordinates. This choice is supported by the timescale of the process we intend to describe,

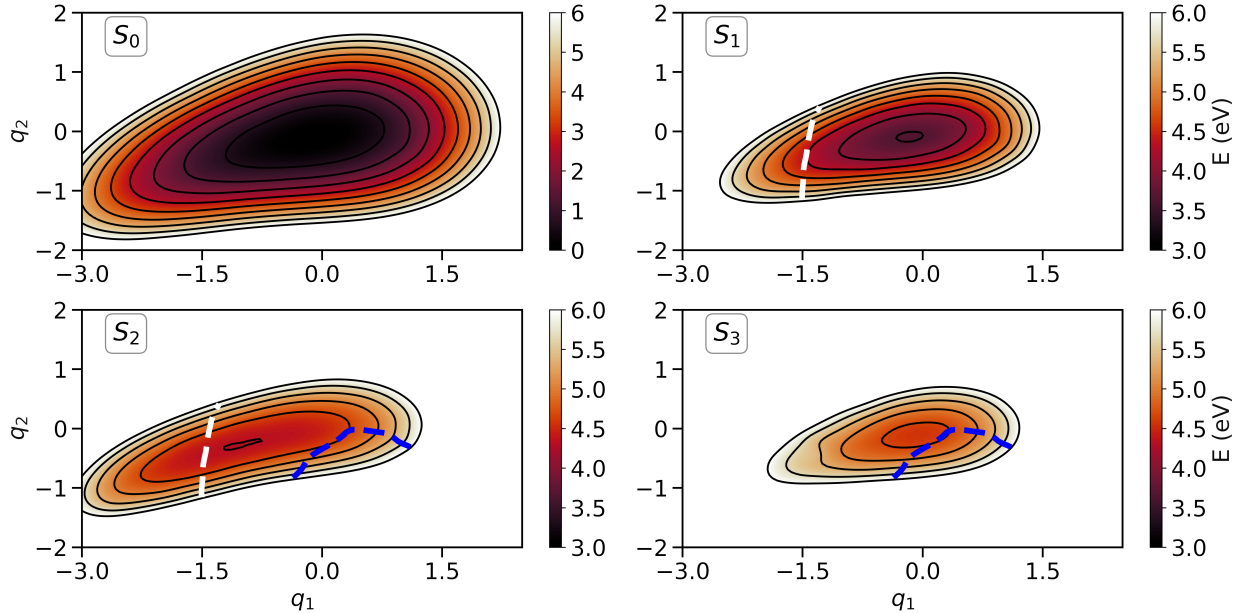


Figure 7. 2D diabatic potential energy surfaces of m-BP. The white dashed line indicates the diabatic intersection seam between S_2 and S_1 including the optimized CoIn. A blue dashed line indicates the diabatic intersection seam between S_3 and S_2 .

specifically the early sub-150-fs dynamics, during which we assume that additional relaxation does not play a dominant role. The diabatic PESs for m-BP are displayed in fig. 7.

D. Quantum Dynamics

The mixed quantum classical excited-state dynamics based on independent trajectories provides a clear picture of the nonadiabatic relaxation events in BP and m-BP. The surface hopping methodology has the ability to tackle the full dimensionality of the nuclear problem; however, it cannot correctly describe coherent superpositions of electronic states. In fact, all dynamics start on a single adiabatic electronic state and not a superposition, such as one created by a laser pulse. Moreover, it does not properly account for decoherence in the nuclear subspace, caused by the nuclear motion. In contrast, an explicit full quantum dynamics simulation correctly describes coherent superpositions and the wave packet branching near a conical intersection, producing a short-lived electronic coherence. Information about the energy gap between the coupled electronic states is encoded in the oscillation period of these transient electronic coherences, and their detection can be used as a direct signature

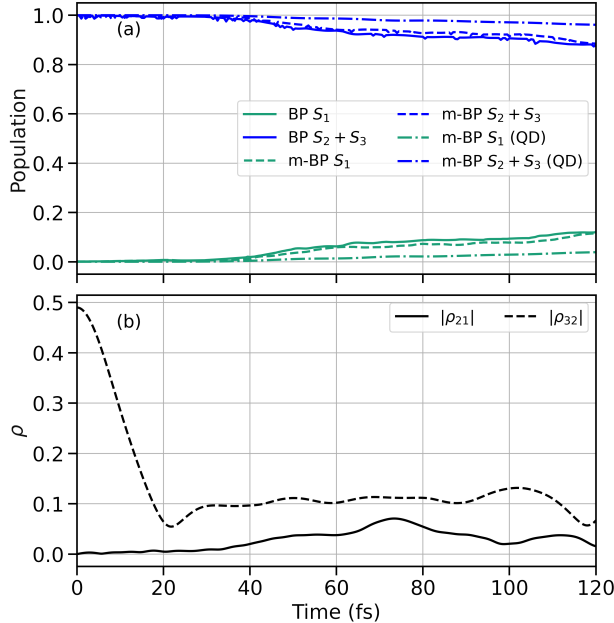


Figure 8. Temporal evolution of diabatic populations and coherences in BP and m-BP during the initial 120 fs. (a): diabatic populations as a function of time, derived from surface hopping (solid and dashed lines) and QD (dash-dotted line) simulations. The populations of S_2 and S_3 are summed together; (b): magnitude of the electronic coherences between S_2 and S_3 as well as S_1 and S_2 . Subscripts indicate the electronic states involved.

of CoIns. However, the grid-based approach we use is only possible for reduced geometric subspaces and not for the full $3N-6$ degrees of freedom. For this reason, we have constructed global PESs in a reduced subspace of the $3N-6$ nuclear d.o.f. of m-BP, and used them for full QD simulations.

Figure 8 displays the temporal evolution of diabatic populations and electronic coherences, ρ , obtained from the QD simulations. The chosen reduced reaction coordinate space can capture the general trend for the S_3 to S_2 internal conversion, as shown in fig. S10 of the SI. However, the S_3/S_2 dynamics are likely washed out by laser pump-pulses longer than 15 fs. Moreover, the electronic coherence generated by the S_3/S_2 CoIn would be largely concealed by the one induced by the pump pulse. Therefore, the populations of S_3 and S_2 are summed in fig. 8. The QD simulations can qualitatively reproduce the population transfer from $S_2 + S_3$ to S_1 predicted by the surface hopping dynamics. In particular, the nonadiabatic relaxation into S_1 begins at 40 fs and displays a similar linear growth. Despite this, there is a quantitative discrepancy in the total population transfer, as QD predicts a

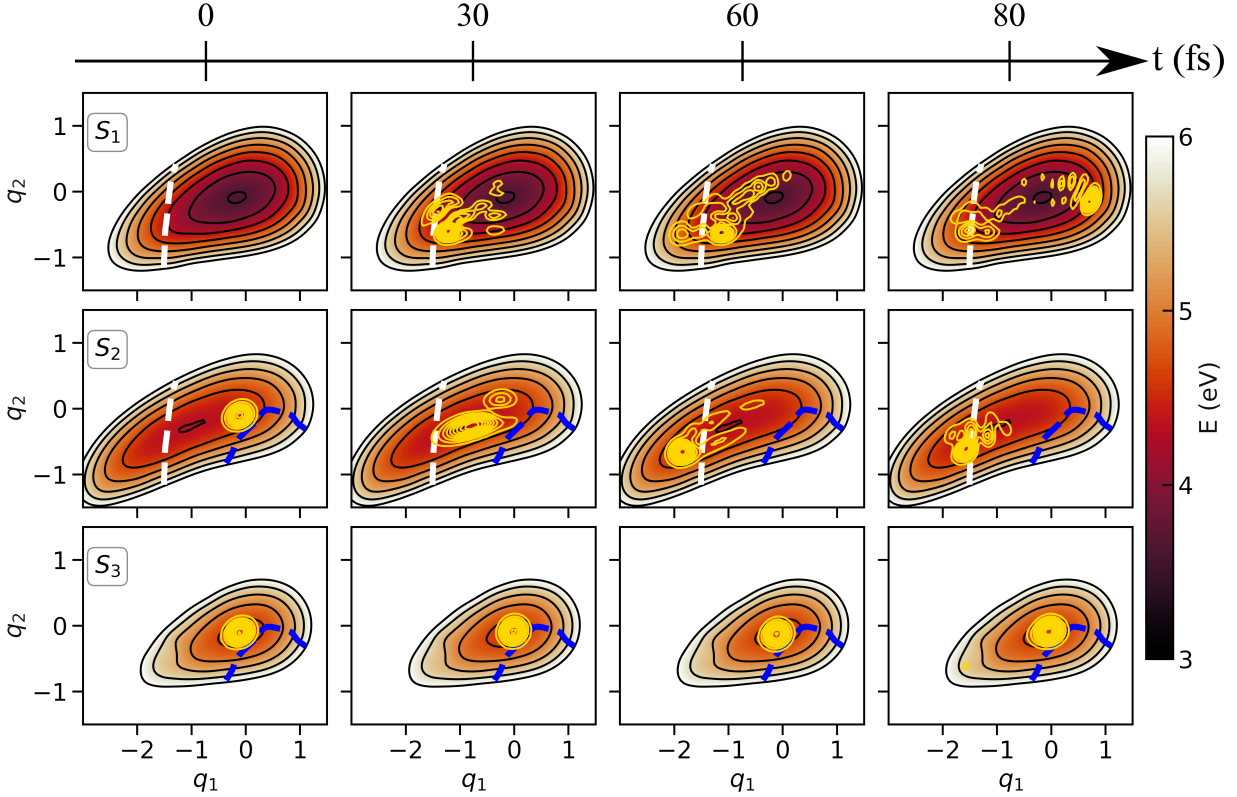


Figure 9. Snapshots of wave packets (gold contour lines) at 0, 30, 60 and 80 fs. First row: wave packet evolution on S_1 ; second row: wave packet evolution on S_2 ; third row: wave packet evolution on S_3 . The white dashed line indicates the diabatic intersection seam between S_2 and S_1 including the optimized CoIn. A blue dashed line indicates the diabatic intersection seam between S_3 and S_2 .

0.05 S_1 population at 100 fs, while the surface hopping dynamics predicts 0.1. A number of factors may account for this: the underlying electronic structure method used in the two approaches (TDA-LR-DFT vs DFT/MRCI) is different; the lack of electronic decoherence in semiclassical trajectory-based dynamics may influence the population transfer directly. The reaction coordinate space used for QD is two-dimensional and does not include all d.o.f. that the system may explore during the time interval of interest. Beyond 120 fs, these differences become more pronounced as the S_1 state is unable to relax within the chosen 2D reaction coordinate space.

Figure 9 shows the time-dependent evolution of the nuclear wave packet on different PESs. Snapshots of the nuclear wave packet density ($|\Psi|^2$) are captured at $t = 0, 30, 60$ and 80 fs.

Since any experimental pump pulse would populate both states, the QD simulations start in a coherent superposition of S_2 and S_3 , thus generating a strong electronic coherence ρ_{32} at 0 fs. This coherence rapidly decays over 20 fs, after which it remains relatively constant around 0.1, with minor oscillations, as illustrated in fig. 8 (b). More interesting is the case of ρ_{21} between S_2 and S_1 . In fact, ρ_{21} is zero for the first 35 fs of the dynamics and begins to increase as the wave packet approaches the CoIn, peaking around 70 fs. The magnitude of ρ_{21} is remarkably large and long-lived (> 50 fs), especially considering that electronic coherences generated by CoIns are typically on the order of 10^{-3} or less [58] and decay very fast. Therefore, the calculated 2D PESs show promise for following studies where ρ_{21} could be probed using time-resolved X-ray techniques [59], such as TRUECARS [60, 61] or time-resolved X-ray absorption spectroscopy. Detection of ρ_{21} could serve as a direct spectroscopic signature of the conical intersection.

IV. CONCLUSION AND OUTLOOK

The excited-state dynamics of gas-phase benzophenone and its alkyl derivative, *meta*-methyl benzophenone have been investigated using mixed quantum classical and full quantum dynamics simulations, focusing on the nonadiabatic processes in the singlet manifold. The mixed quantum classical simulations were carried out at the Tamm-Dancoff approximation linear response density functional theory level of theory using a surface hopping approach. The electronic structure method was benchmarked against experimental and theoretical data, assuring a qualitatively correct description of all states involved. We were able to analyze the excited state dynamics for BP and m-BP for 500 fs, observing both the non-adiabatic relaxation process from S_3 to S_2 and then from S_2 to S_1 . In addition to discussing the geometrical relaxation and the population dynamics, we also simulate an experimentally accessible observable, namely time-resolved photoelectron spectra for both molecules.

In both cases, we observe an exponential decay of the population in the S_3 . This behavior is observed in the time-resolved photoelectron spectra as a blueshift of 0.4 eV within the first 15 fs, immediately followed by an interchange in the intensity profile of the photoelectron bands. The population transfer to S_1 starts around 40 fs, and the increase/decrease in the population of S_1/S_2 is linear. As the system passes through the S_2/S_1 conical intersection,

a bifurcation in the photoelectron signal appears in the spectra, followed by a linear increase in the S_1 band and a decrease in the intensity of the S_2 signal.

To gain more insight and to correctly describe electronic coherences and superpositions of electronic states, we computed two-dimensional potential energy surfaces for *meta*-methylbenzophenone to perform full quantum dynamics simulations. The presence of the methyl group in the *meta* position increases the energy gap between the S_3 to S_2 states, which, however, only marginally affects the excited-state dynamics compared to BP. This separation is in turn beneficial, as it leads to a slight decoupling of the two states at the Frank-Condon point, allowing for reasonable diabaticization. The quantum dynamics simulations, carried out in a subspace of the full dimensional problem and in a diabatic basis, qualitatively reproduce the surface hopping dynamics over the first 120 fs of propagation. While the relaxation timescale and linear population increase are accurately depicted, surface hopping and quantum dynamics simulations differ quantitatively. The former predicts a population of 0.1 in S_1 at 100 fs, whereas the latter predicts 0.05. The discrepancy between the two approaches may be attributed to a number of factors, including the differing electronic structure theories employed, and the reduced reaction coordinate space utilized in quantum dynamics. The electronic coherence generated by the bifurcation of the nuclear wave packet at the S_2/S_1 conical intersection is remarkably large and survives for more than 50 fs. Consequently, the selected coordinate subspace appears promising for future investigations in which the electronic coherence might be probed with more advanced time-resolved X-ray techniques, which rely on electronic coherences.

ACKNOWLEDGMENTS

This project has received funding from the European Research Council (ERC) under the European Union’s Horizon 2020 research and innovation program (grant agreement no. 852286). Support from the Swedish Research Council (Grant No. VR 2022-05005) is acknowledged. L.R. thanks Sambit Das for the many scientific discussions on surface hopping.

SUPPORTING INFORMATION

See the Supporting information for additional benchmarking of vertical excitations of benzophenone using CASSCF and RASSCF; natural orbital plots of the active spaces used in the calculations; normal mode analysis of SHARC trajectories for the first 150 fs; average temporal evolution of selected geometric parameters of benzophenone and *meta*-methyl benzophenone.

AUTHOR DECLARATION SECTION

Conflict of Interest Statement

The authors have no conflicts to disclose.

Author Contributions

Lorenzo Restaino: Data curation (lead); Investigation (lead); Visualization (lead); Writing – original draft (lead); Writing – review & editing (equal). **Thomas Schnappinger:** Conceptualization (equal); Investigation (supporting); Supervision (equal); Writing – original draft (supporting); Writing – review & editing (equal). **Markus Kowalewski:** Conceptualization (equal); Funding acquisition (lead); Project administration (lead); Supervision (equal); Writing – original draft (supporting); Writing – review & editing (equal).

DATA AVAILABILITY

The data that support the findings of this study are available from the corresponding author upon reasonable request.

-
- [1] Sae Youn Lee, Takuma Yasuda, Yu Seok Yang, Qisheng Zhang, and Chihaya Adachi. Luminous butterflies: efficient exciton harvesting by benzophenone derivatives for full-color delayed fluorescence OLEDs. *Angew. Chem. Int. Ed Engl.*, 53(25):6402–6406, June 2014.

- [2] Samik Jhulki, Saona Seth, Avijit Ghosh, Tahsin J Chow, and Jarugu Narasimha Moorthy. Benzophenones as generic host materials for phosphorescent organic light-emitting diodes. *ACS Appl. Mater. Interfaces*, 8(2):1527–1535, January 2016.
- [3] Chun-Xiang Li, Wei-Wei Guo, Bin-Bin Xie, and Ganglong Cui. Photodynamics of oxybenzone sunscreen: Nonadiabatic dynamics simulations. *J. Chem. Phys.*, 145(7), August 2016.
- [4] Natalie G K Wong, Conor D Rankine, and Caroline E H Dessent. Linking electronic relaxation dynamics and ionic photofragmentation patterns for the deprotonated UV filter benzophenone-4. *J. Phys. Chem. Lett.*, 12(11):2831–2836, March 2021.
- [5] M Consuelo Cuquerella, Virginie Lhiaubet-Vallet, Jean Cadet, and Miguel A Miranda. Benzophenone photosensitized DNA damage. *Acc. Chem. Res.*, 45(9):1558–1570, September 2012.
- [6] Elise Dumont, Meilani Wibowo, Daniel Roca-Sanjuán, Marco Garavelli, Xavier Assfeld, and Antonio Monari. Resolving the benzophenone DNA-photosensitization mechanism at QM/MM level. *J. Phys. Chem. Lett.*, 6(4):576–580, February 2015.
- [7] Stéphane Aloïse, Cyril Ruckebusch, Lionel Blanchet, Julien Réhault, Guy Buntinx, and Jean-Pierre Huvenne. The benzophenone $S_1(n,\pi^*) \rightarrow T_1(n,\pi^*)$ states intersystem crossing reinvestigated by ultrafast absorption spectroscopy and multivariate curve resolution. *J. Phys. Chem. A*, 112(2):224–231, January 2008.
- [8] Gloria Spighi, Marc-André Gaveau, Jean-Michel Mestdagh, Lionel Poisson, and Benoît Soep. Gas phase dynamics of triplet formation in benzophenone. *Phys. Chem. Chem. Phys.*, 16(20):9610–9618, May 2014.
- [9] Dumitru-Claudiu Sergentu, Rémi Maurice, Remco W A Havenith, Ria Broer, and Daniel Roca-Sanjuán. Computational determination of the dominant triplet population mechanism in photoexcited benzophenone. *Phys. Chem. Chem. Phys.*, 16(46):25393–25403, December 2014.
- [10] Lucilla Favero, Giovanni Granucci, and Maurizio Persico. Surface hopping investigation of benzophenone excited state dynamics. *Phys. Chem. Chem. Phys.*, 18(15):10499–10506, April 2016.
- [11] Marco Marazzi, Sebastian Mai, Daniel Roca-Sanjuán, Mickaël G Delcey, Roland Lindh, Leticia González, and Antonio Monari. Benzophenone Ultrafast Triplet Population: Revisiting the Kinetic Model by Surface-Hopping Dynamics. *J. Phys. Chem. Lett.*, 7(4):622–626, February 2016.

- [12] Katsuyuki Shizu and Hironori Kaji. Theoretical determination of rate constants from excited states: Application to benzophenone. *J. Phys. Chem. A*, 125(40):9000–9010, October 2021.
- [13] Bipin K Shah, Michael A J Rodgers, and Douglas C Neckers. The S₂ → S₁ Internal Conversion of Benzophenone and p-Iodobenzophenone. *J. Phys. Chem. A*, 108(29):6087–6089, July 2004.
- [14] Markus Kowalewski and Phillip Seeber. Sustainable packaging of quantum chemistry software with the Nix package manager. *Int. J. Quantum Chem.*, 122(9), May 2022.
- [15] Jeng-Da Chai and Martin Head-Gordon. Systematic optimization of long-range corrected hybrid density functionals. *J. Chem. Phys.*, 128(8):084106, February 2008.
- [16] Stefan Grimme. Semiempirical GGA-type density functional constructed with a long-range dispersion correction. *J. Comput. Chem.*, 27(15):1787–1799, November 2006.
- [17] R Krishnan, J S Binkley, R Seeger, and J A Pople. Self-consistent molecular orbital methods. XX. A basis set for correlated wave functions. *J. Chem. Phys.*, 72(1):650–654, January 1980.
- [18] M J Frisch, G W Trucks, H B Schlegel, G E Scuseria, M A Robb, J R Cheeseman, G Scalmani, V Barone, G A Petersson, H Nakatsuji, X Li, M Caricato, A V Marenich, J Bloino, B G Janesko, R Gomperts, B Mennucci, H P Hratchian, J V Ortiz, A F Izmaylov, J L Sonnenberg, D Williams-Young, F Ding, F Lipparini, F Egidi, J Goings, B Peng, A Petrone, T Henderson, D Ranasinghe, V G Zakrzewski, J Gao, N Rega, G Zheng, W Liang, M Hada, M Ehara, K Toyota, R Fukuda, J Hasegawa, M Ishida, T Nakajima, Y Honda, O Kitao, H Nakai, T Vreven, K Throssell, J A Montgomery, Jr, J E Peralta, F Ogliaro, M J Bearpark, J J Heyd, E N Brothers, K N Kudin, V N Staroverov, T A Keith, R Kobayashi, J Normand, K Raghavachari, A P Rendell, J C Burant, S S Iyengar, J Tomasi, M Cossi, J M Millam, M Klene, C Adamo, R Cammi, J W Ochterski, R L Martin, K Morokuma, O Farkas, J B Foresman, and D J Fox. Gaussian 16 Revision C.01, 2016.
- [19] So Hirata and Martin Head-Gordon. Time-dependent density functional theory within the Tamm–Dancoff approximation. *Chem. Phys. Lett.*, 314(3):291–299, December 1999.
- [20] Asim Najibi and Lars Goerigk. DFT-D4 counterparts of leading meta-generalized-gradient approximation and hybrid density functionals for energetics and geometries. *J. Comput. Chem.*, 41(30):2562–2572, November 2020.
- [21] Frank Neese. The ORCA program system. *Wiley Interdiscip. Rev. Comput. Mol. Sci.*, 2(1):73–78, January 2012.

- [22] Frank Neese. Software update: The ORCA program system—Version 5.0. *Wiley Interdiscip. Rev. Comput. Mol. Sci.*, 12(5), September 2022.
- [23] F. Aquilante, J. Autschbach, A. Baiardi, S. Battaglia, V. A. Borin, L. F. Chibotaru, I. Conti, L. De Vico, M. Delcey, I. Fdez. Galván, N. Ferré, L. Freitag, M. Garavelli, X. Gong, S. Knecht, Ernst D. Larsson, R. Lindh, M Lundberg P.-Å. Malmqvist, , A. Nenov, J. Norell, M Odelius, M. Olivucci, T. B. Pedersen, L. Pedraza-González, Q. M. Phung, K. Pierloot, M. Reiher, I. Schapiro, J. Segarra-Martí, F. Segatta, L. Seijo, S. Sen, D.-C. Sergentu, C. J. Stein, L. Ungur, M. Vacher, A. Valentini, and V. Veryazov. Modern Quantum Chemistry with [Open]Molcas. *J. Chem. Phys.*, 152:214117, 2020.
- [24] Giovanni Li Manni, Ignacio Fdez Galván, Ali Alavi, Flavia Aleotti, Francesco Aquilante, Jochen Autschbach, Davide Avagliano, Alberto Baiardi, Jie J Bao, Stefano Battaglia, Letitia Birnoschi, Alejandro Blanco-González, Sergey I Bokarev, Ria Broer, Roberto Cacciari, Paul B Calio, Rebecca K Carlson, Rafael Carvalho Couto, Luis Cerdán, Liviu F Chibotaru, Nicholas F Chilton, Jonathan Richard Church, Irene Conti, Sonia Coriani, Juliana Cuéllar-Zuquin, Razan E Daoud, Nike Dattani, Piero Decleva, Coen de Graaf, Mickaël G Delcey, Luca De Vico, Werner Dobrautz, Sijia S Dong, Rulin Feng, Nicolas Ferré, Michael Filatov Gulak, Laura Gagliardi, Marco Garavelli, Leticia González, Yafu Guan, Meiyuan Guo, Matthew R Hennefarth, Matthew R Hermes, Chad E Hoyer, Miquel Huix-Rotllant, Vishal Kumar Jaiswal, Andy Kaiser, Danil S Kaliakin, Marjan Khamesian, Daniel S King, Vladislav Kochetov, Marek Krośnicki, Arpit Arun Kumaar, Ernst D Larsson, Susi Lehtola, Marie-Bernadette Lepetit, Hans Lischka, Pablo López Ríos, Marcus Lundberg, Dongxia Ma, Sebastian Mai, Philipp Marquetand, Isabella C D Merritt, Francesco Montorsi, Maximilian Mörchen, Artur Nenov, Vu Ha Anh Nguyen, Yoshio Nishimoto, Meagan S Oakley, Massimo Olivucci, Markus Oppel, Daniele Padula, Riddhish Pandharkar, Quan Manh Phung, Felix Plasser, Gerardo Raggi, Elisa Rebolini, Markus Reiher, Ivan Rivalta, Daniel Roca-Sanjuán, Thies Romig, Arta Anushirwan Safari, Aitor Sánchez-Mansilla, Andrew M Sand, Igor Schapiro, Thais R Scott, Javier Segarra-Martí, Francesco Segatta, Dumitru-Claudiu Sergentu, Prachi Sharma, Ron Shepard, Yanan Shu, Jakob K Staab, Tjerk P Straatsma, Lasse Kragh Sørensen, Bruno Nunes Cabral Tenorio, Donald G Truhlar, Liviu Ungur, Morgane Vacher, Valera Veryazov, Torben Arne Voß, Oskar Weser, Dihua Wu, Xuchun Yang, David Yarkony, Chen Zhou, J Patrick Zobel, and Roland Lindh. The OpenMolcas web: A community-driven approach to advancing computational

- chemistry. *J. Chem. Theory Comput.*, 19(20):6933–6991, October 2023.
- [25] Per-Olof Widmark, Per-Åke Malmqvist, and Björn O Roos. Density matrix averaged atomic natural orbital (ANO) basis sets for correlated molecular wave functions. *Theor. Chim. Acta*, 77(5):291–306, September 1990.
- [26] Toru Shiozaki, Werner Gyorffy, Paolo Celani, and Hans-Joachim Werner. Communication: extended multi-state complete active space second-order perturbation theory: energy and nuclear gradients. *J. Chem. Phys.*, 135(8):081106, August 2011.
- [27] Alexander A Granovsky. Extended multi-configuration quasi-degenerate perturbation theory: the new approach to multi-state multi-reference perturbation theory. *J. Chem. Phys.*, 134(21):214113, June 2011.
- [28] Stefan Grimme and Mirko Waletzke. A combination of Kohn–Sham density functional theory and multi-reference configuration interaction methods. *J. Chem. Phys.*, 111(13):5645–5655, October 1999.
- [29] Simon P Neville and Michael S Schuurman. A perturbative approximation to DFT/MRCI: DFT/MRCI(2). *J. Chem. Phys.*, 157(16):164103, October 2022.
- [30] Teagan Shane Costain, Victoria Ogden, Simon P Neville, and Michael S Schuurman. A DFT/MRCI Hamiltonian parameterized using only ab initio data: I. valence excited states. *J. Chem. Phys.*, 160(22):224106, June 2024.
- [31] Yifan Jin and Rodney J Bartlett. Accurate computation of X-ray absorption spectra with ionization potential optimized global hybrid functional. *J. Chem. Phys.*, 149(6):064111, August 2018.
- [32] Simon P Neville and Michael S Schuurman. Calculation of quasi-diabatic states within the DFT/MRCI(2) framework: The QD-DFT/MRCI(2) method. *J. Chem. Phys.*, 160(23):234109, June 2024.
- [33] S Neville and M Schuurman. GRaCI: General Reference Configuration Interaction, October 2021.
- [34] Markus Kowalewski, Elisabeth Larsson, and Alfa Heryudono. An adaptive interpolation scheme for molecular potential energy surfaces. *J. Chem. Phys.*, 145(8):084104, August 2016.
- [35] Sebastian Mai, Philipp Marquetand, and Leticia González. Nonadiabatic Dynamics: The SHARC Approach. *WIREs Comput. Mol. Sci.*, 8:e1370, 2018.

- [36] Sebastian Mai, Davide Avagliano, Moritz Heindl, Philipp Marquetand, Maximilian F S J Menger, Markus Oppel, Felix Plasser, Severin Polonius, Matthias Ruckebauer, Yinan Shu, Donald G Truhlar, Linyao Zhang, Patrick Zobel, and Leticia González. SHARC3.0: Surface Hopping Including Arbitrary Couplings — Program Package for Non-Adiabatic Dynamics. <https://sharc-md.org/>, 2023.
- [37] Sebastian Mai, Philipp Marquetand, Martin Richter, Jesús González-Vázquez, and Leticia González. Singlet and triplet excited-state dynamics study of the keto and enol tautomers of cytosine. *ChemPhysChem*, 14(13):2920–2931, sep 2013.
- [38] Sebastian Mai, Philipp Marquetand, and Leticia González. A general method to describe intersystem crossing dynamics in trajectory surface hopping. *Int. J. Quantum Chem.*, 115:1215–1231, 2015.
- [39] Giovanni Granucci and Maurizio Persico. Critical appraisal of the fewest switches algorithm for surface hopping. *J. Chem. Phys.*, 126(13):134114, April 2007.
- [40] Felix Plasser, Matthias Ruckebauer, Sebastian Mai, Markus Oppel, Philipp Marquetand, and Leticia González. Efficient and flexible computation of many-electron wave function overlaps. *J. Chem. Theory Comput.*, 12(3):1207–1219, 2016.
- [41] Giovanni Granucci, Maurizio Persico, and Alberto Zocante. Including quantum decoherence in surface hopping. *J. Chem. Phys.*, 133(13):134111, October 2010.
- [42] Matthias Ruckebauer, Sebastian Mai, Philipp Marquetand, and Leticia González. Revealing deactivation pathways hidden in time-resolved photoelectron spectra. *Sci. Rep.*, 6(1):35522, October 2016.
- [43] Feit, J A Fleck, and A Steiger. Solution of the Schrödinger equation by a spectral method. *J. Comput. Phys.*, 47(3):412–433, September 1982.
- [44] D Kosloff and R Kosloff. A fourier method solution for the time dependent Schrödinger equation as a tool in molecular dynamics. *J. Comput. Phys.*, 52(1):35–53, October 1983.
- [45] David J Tannor. *Introduction to Quantum Mechanics: A Time-Dependent Perspective*. January 2007.
- [46] M Kowalewski and R de Vivie-Riedle. QDng: A Grid Based Molecular Quantum Dynamics Package, April 2024.
- [47] Jernej Stare and Gabriel G Balint-Kurti. Fourier Grid Hamiltonian Method for Solving the Vibrational Schrödinger Equation in Internal Coordinates: Theory and Test Applications. *J.*

- Phys. Chem. A*, 107(37):7204–7214, September 2003.
- [48] Cornelius Lanczos. An iteration method for the solution of the eigenvalue problem of linear differential and integral operators. *J. Res. Natl. Bur. Stand. B*, 45:255–282, 1950.
- [49] Tae Jun Park and J C Light. Unitary quantum time evolution by iterative Lanczos reduction. *J. Chem. Phys.*, 85(10):5870–5876, November 1986.
- [50] Marlis Hochbruck and Christian Lubich. On Krylov Subspace Approximations to the Matrix Exponential Operator. *SIAM Journal on Numerical Analysis*, July 2006.
- [51] Takao Itoh. Emission characteristics of benzophenone vapor at low pressure. *J. Phys. Chem.*, 89(19):3949–3951, September 1985.
- [52] G Centineo, I Fragala’, G Bruno, and S Spampinato. Photoelectron spectroscopy of benzophenone, acetophenone and their ortho-alkyl derivatives. *J. Mol. Struct.*, 44(2):203–210, April 1978.
- [53] E J McAlduff and D L Bunbury. Photoelectron spectra of some aromatic mono- and di-ketones. *J. Electron Spectrosc. Relat. Phenom.*, 17(2):81–89, January 1979.
- [54] Noura Khemiri, Sabri Messaoudi, Manef Abderrabba, Gloria Spighi, Marc-André Gaveau, Marc Briant, Benoît Soep, Jean-Michel Mestdagh, Majdi Hochlaf, and Lionel Poisson. Photoionization of benzophenone in the gas phase: Theory and experiment. *J. Phys. Chem. A*, 119(23):6148–6154, June 2015.
- [55] Zied Gouid, Anja Röder, Barbara K Cunha de Miranda, Marc-André Gaveau, Marc Briant, Benoît Soep, Jean-Michel Mestdagh, Majdi Hochlaf, and Lionel Poisson. Energetics and ionization dynamics of two diarylketone molecules: benzophenone and fluorenone. *Phys. Chem. Chem. Phys.*, 21(26):14453–14464, July 2019.
- [56] Carl Eckart. Some Studies Concerning Rotating Axes and Polyatomic Molecules. *Phys. Rev.*, 47(7):552–558, April 1935.
- [57] James D Louck and Harold W Galbraith. Eckart vectors, Eckart frames, and polyatomic molecules. *Rev. Mod. Phys.*, 48(1):69–106, January 1976.
- [58] Simon P Neville, Albert Stolow, and Michael S Schuurman. Formation of electronic coherences in conical intersection-mediated dynamics. *J. Phys. B At. Mol. Opt. Phys.*, 55(4):044004, February 2022.
- [59] Thomas Schnappinger, Deependra Jadoun, Mahesh Gudem, and Markus Kowalewski. Time-resolved X-ray and XUV based spectroscopic methods for nonadiabatic processes in photo-

- chemistry. *Chem. Commun.*, 58(92):12763–12781, November 2022.
- [60] Markus Kowalewski, Kochise Bennett, Konstantin E Dorfman, and Shaul Mukamel. Catching Conical Intersections in the Act: Monitoring Transient Electronic Coherences by Attosecond Stimulated X-Ray Raman Signals. *Phys. Rev. Lett.*, 115(19):193003, November 2015.
- [61] Lorenzo Restaino, Deependra Jadoun, and Markus Kowalewski. Probing nonadiabatic dynamics with attosecond pulse trains and soft x-ray Raman spectroscopy. *Struct Dyn*, 9(3):034101, May 2022.

**Supporting Informations: Simulating Nonadiabatic Dynamics in
Benzophenone: Tracing Internal Conversion Through
Photoelectron Spectra**

Lorenzo Restaino, Thomas Schnappinger, and Markus Kowalewski*

Department of Physics, Stockholm University,

Albanova University Centre, SE-106 91 Stockholm, Sweden

arXiv:2411.14134v1 [physics.chem-ph] 21 Nov 2024

* e-mail: markus.kowalewski@fysik.su.se

CONTENTS

S1 . Additional Benchmark of Vertical Excitation Energies	3
A. CASPT2	3
B. RASPT2	6
S2 . DFT/MRCI Active Space	8
S3 . Normal Mode Analysis with SHARC	10
S4 . Potential Energy surfaces	12
S5 . SHARC Populations of BP and m-BP	13
References	14

S1 . ADDITIONAL BENCHMARK OF VERTICAL EXCITATION ENERGIES

A. CASPT2

Benzophenone in its ground state is a non-planar molecule with C_2 symmetry. The steric repulsion of hydrogen atoms causes rotation between the phenyl rings. We noticed that, starting from the actual twisted structure, the calculations produce incorrect S_0 and S_1 state energies. To correct for this, we first carried out a single-point CASSCF calculation on the planar structure and then used the resulting RasOrb file on the twisted ground-state structure.

Table S1. Additional benchmark of vertical energies (eV) for gas-phase benzophenone.

	CASPT2(12,11)		CASPT2(14,13)		CASPT2(16,15)		CCSD ^a	TDA ^b	Exp.
	4avg	5avg	4avg	5avg	4avg	5avg			
$S_0 \rightarrow S_1$	3.57	3.66	3.57	3.65	3.53	3.65	3.69	3.98	3.61 ^c
$S_0 \rightarrow S_2$	4.96	5.20	4.59	4.59	4.60	4.60	4.60	5.28	4.40 ^c
$S_0 \rightarrow S_3$	4.99	5.24	4.89	4.88	4.67	4.62	4.67	5.32	4.40
$S_0 \rightarrow S_4$		5.56		5.83		5.83	5.47	5.62	5.00

^a STEOM-DLPNO-CCSD/def2-TZVP; ^b ω B97-D3/6-311G*; ^c low pressure vapor, ref. [1].

Table S2. Oscillator strength of the vertical transitions reported in table S1.

	CASPT2(12,11)		CASPT2(14,13)		CASPT2(16,15)		CCSD ^a	TDA ^b	Exp.
	4avg	5avg	4avg	5avg	4avg	5avg			
$S_0 \rightarrow S_1$	0.0009	0.0010	0.0010	0.0009	0.0009	0.0007	0.0008	0.0011	weak
$S_0 \rightarrow S_2$	0.0048	0.0062	0.0021	0.0033	0.0014	0.0036	0.0080	0.0165	
$S_0 \rightarrow S_3$	0.0034	0.0104	0.0044	0.0059	0.0027	0.0023	0.0058	0.0164	
$S_0 \rightarrow S_4$		0.0032		0.0145		0.0068	0.5067	0.4387	strong

^a ω B97-D3/6-311G*; ^b STEOM-DLPNO-CCSD/def2-TZVP.

Sergentu et al. [2] calculated a minimum energy path (MEP) at the CASPT2 level on a CAS(12,11) wave function with the ANO-L-VDZP basis set and stated that it does not lead to the S_2/S_1 conical intersection reporting an energy splitting of 0.69 eV. They concluded

RAS2

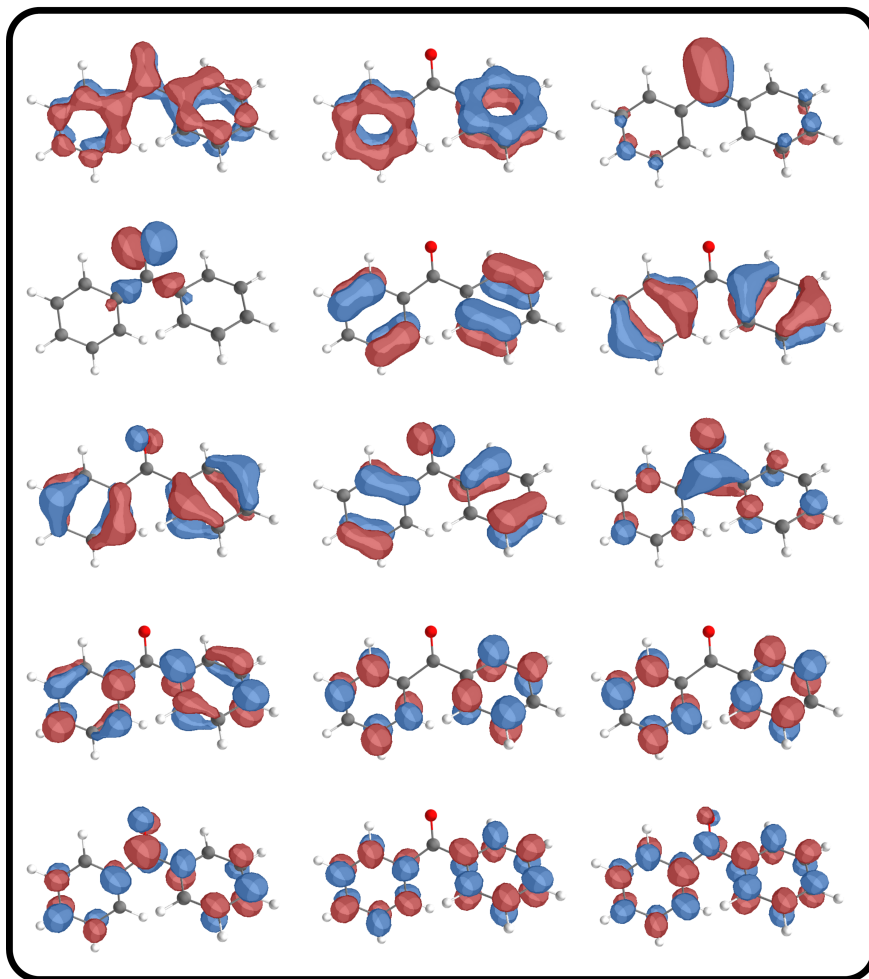


Figure S1. Natural orbitals of benzophenone in the active space with 16 electrons in 15 orbitals, calculated at the CAS(16,16)/ANO-L-VDZP level of theory.

that CAS(12,11) is inadequate to describe the state S_2 due to the absence of the lowest π orbitals and corresponding π^* in the active space. We agree that an accurate characterization of the S_2 PES is crucial for understanding the photoexcitation dynamics, though our results differ slightly from their findings. In their paper, they did not specify which CASPT2 variant was used, but our replication of their results was successful only with multi-state (MS) CASPT2.

We employed extended multi-state CASPT2 (XMS-CASPT2), which provides a better description of the states, particularly when state mixing is strong. Our benchmarks for gas-phase benzophenone vertical energies are in table S1. The analysis of the CI coefficients for S_2 , S_3 , and S_4 did not show significant contributions from the two lowest π orbitals,

suggesting that the improved description of S_2 is simply due to a larger active space, where the correlation of the π -system is better. This is evident in tables S1 and S3. The S_1 state is unaffected by the active space size, but slightly influenced by the state-averaging number, with differences under 0.1 eV. The smaller active space (12,11) inadequately describes S_2 , showing differences over 0.4 eV compared to the largest active space. So the conclusion reached by Sergentu et al. regarding this state still holds true.

B. RASPT2

We have also benchmarked vertical excitations in the single manifold with RASPT2 [3, 4]. The energies and the corresponding oscillator strength are reported in tables S3. and S4.

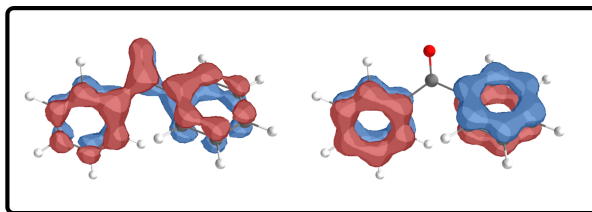
Table S3. Benchmark of vertical energies (eV) for gas-phase benzophenone using XMS-RASPT2, with 2 orbitals in the RAS1, 11 orbitals in the RAS2 and 2 orbitals in the RAS3. One hole and one particle are allowed in the RAS1 and RAS3, respectively.

	RASPT2		CASPT2(16,15)		Exp.
	4avg	5avg	4avg	5avg	
$S_0 \rightarrow S_1$	3.83	3.65	3.53	3.65	3.61
$S_0 \rightarrow S_2$	4.61	4.67	4.60	4.60	4.40
$S_0 \rightarrow S_3$	4.63	4.67	4.67	4.62	4.40
$S_0 \rightarrow S_4$		5.80		5.83	5.00

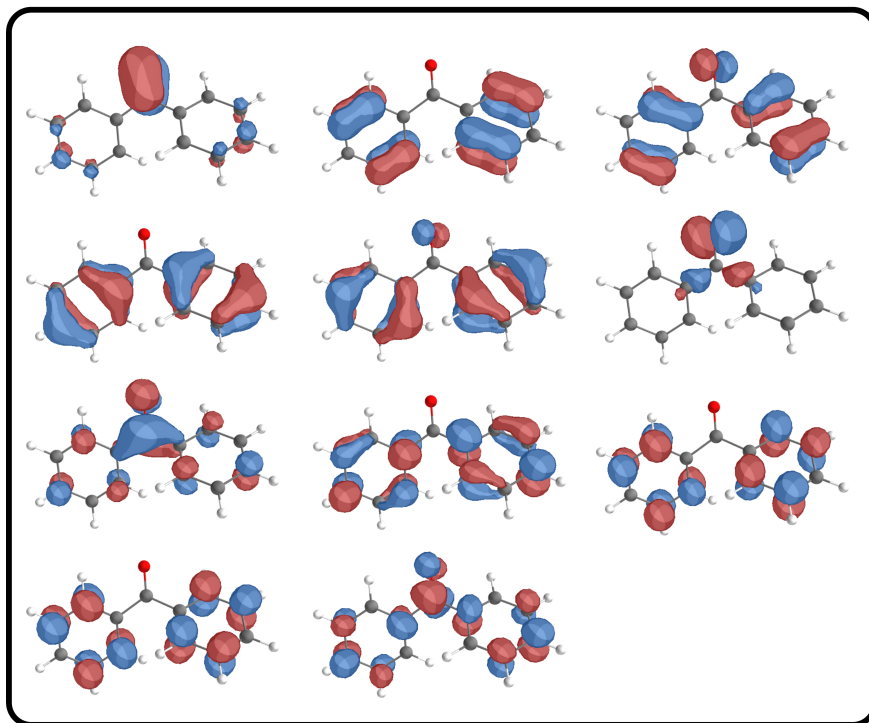
Table S4. Oscillator strength of the vertical transitions reported in table S3.

	RASPT2		CASPT2(16,15)		Exp.
	4avg	5avg	4avg	5avg	
$S_0 \rightarrow S_1$	0.0013	0.0009	0.0009	0.0007	weak
$S_0 \rightarrow S_2$	0.0042	0.0049	0.0014	0.0036	
$S_0 \rightarrow S_3$	0.0017	0.0032	0.0027	0.0023	
$S_0 \rightarrow S_4$		0.0082		0.0068	strong

RAS1



RAS2



RAS3

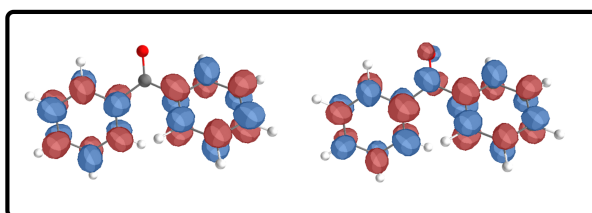


Figure S2. Natural orbitals of benzophenone in the restricted active space formalism with two orbitals in the RAS1, 11 orbitals in the RAS2, and two orbitals in the RAS3. 12 electrons in the RAS2, one hole and one particle allowed in the RAS1 and RAS3 respectively.

S2 . DFT/MRCI ACTIVE SPACE

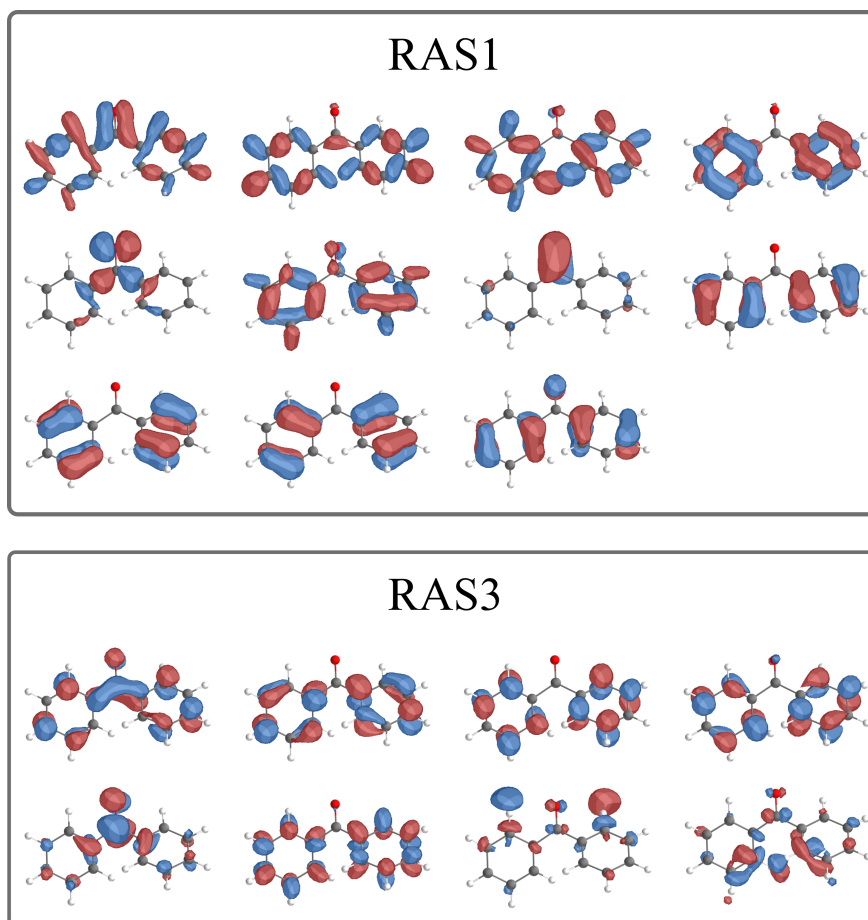


Figure S3. Natural orbitals of benzophenone in the active space used in DFT/MRCI calculations. Two holes and two particles are allowed in the RAS1 and RAS3 respectively.

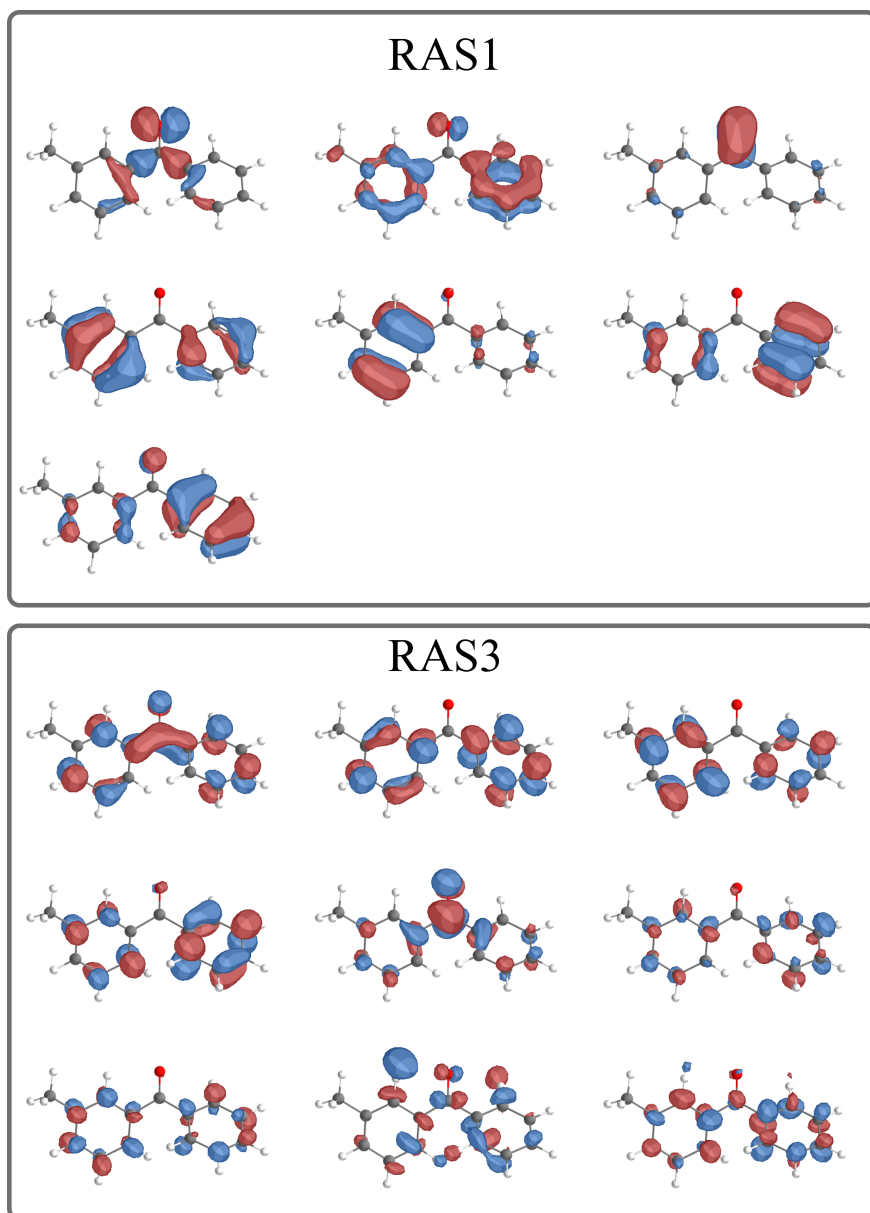


Figure S4. Natural orbitals of *meta*-methyl benzophenone in the active space used in DFT/MRCI calculations. Two holes and two particles are allowed in the RAS1 and RAS3 respectively.

S3 . NORMAL MODE ANALYSIS WITH SHARC

The activity of the normal modes of BP and m-BP for their respective ensemble of trajectories was calculated as implemented in SHARC [5]. We restrict our analysis to the first 150 fs of the dynamics.

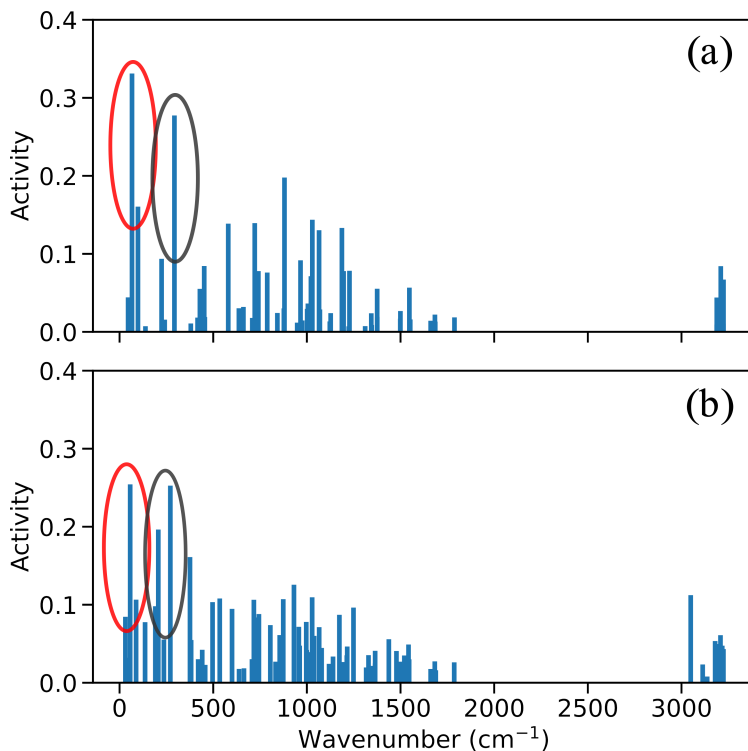


Figure S5. Normal mode analysis of the average trajectory for (a) benzophenone and (b) *meta*-methyl benzophenone, for the first 150 fs of the dynamics. Red oval indicate normal modes associated with the dihedral motion of the two aryl rings. Grey oval indicate normal modes associated with C-C stretching involving the carbon atom of the carbonyl group.

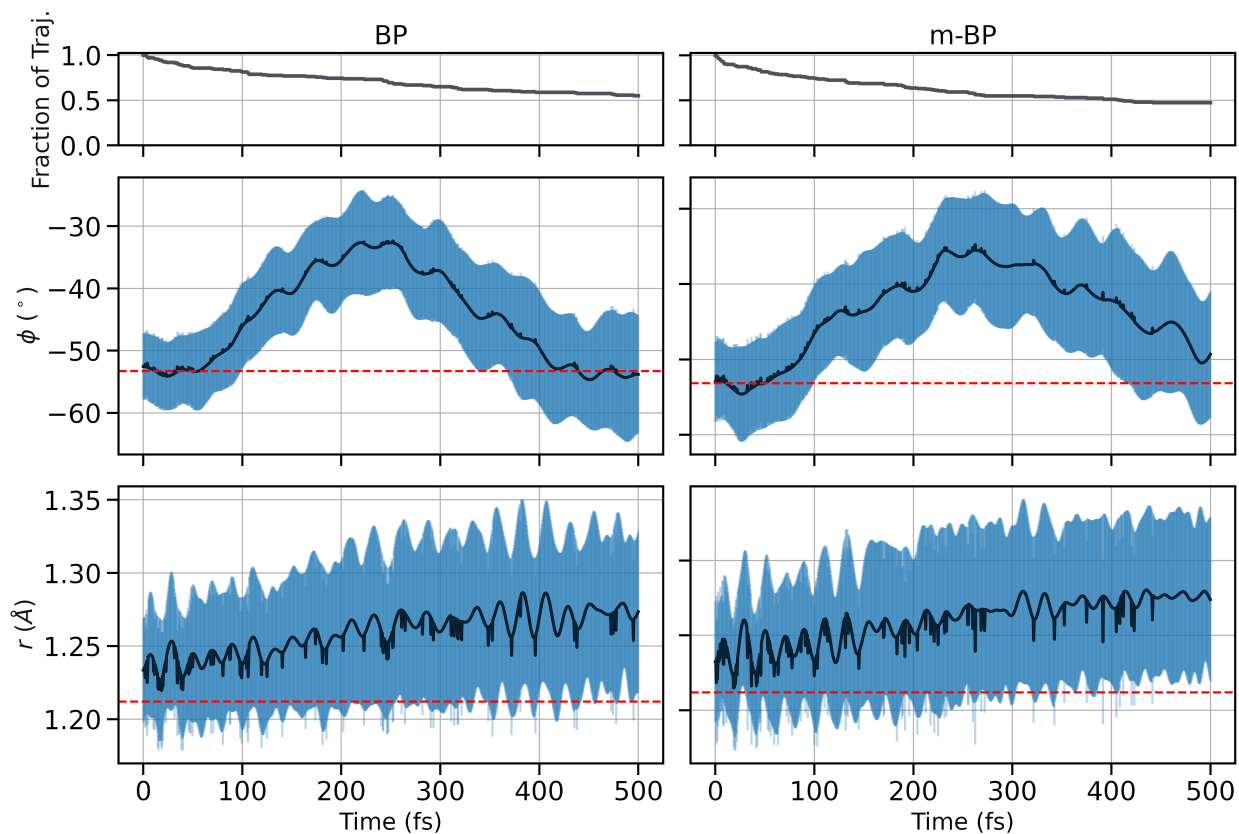


Figure S6. Mean progression of geometric parameters over time for BP (left column) and m-BP (right column). Top panel: fraction of trajectories (grey line) meeting the total energy conservation criteria at each time step; middle panel: mean temporal progression of the dihedral angle between the two aryl rings; bottom panel: mean temporal progression of the CO bond length. Red dashed lines indicate values at the FC point.

S4 . POTENTIAL ENERGY SURFACES

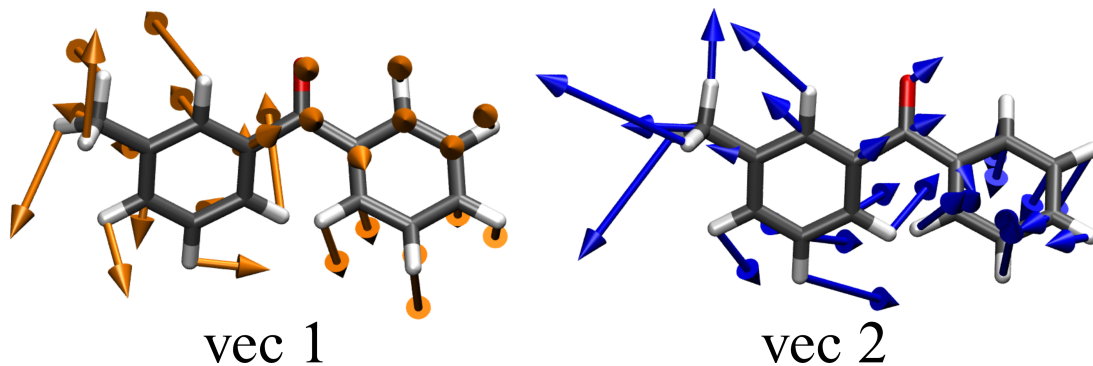


Figure S7. Graphical depiction of the orthonormalized vectors spanning the coordinate space used to form potential energy surfaces for m-BP. Vec1 represents the difference vector between the FC geometry and the CoIn geometry. Vec2 represents the dihedral angle between the aryl rings.

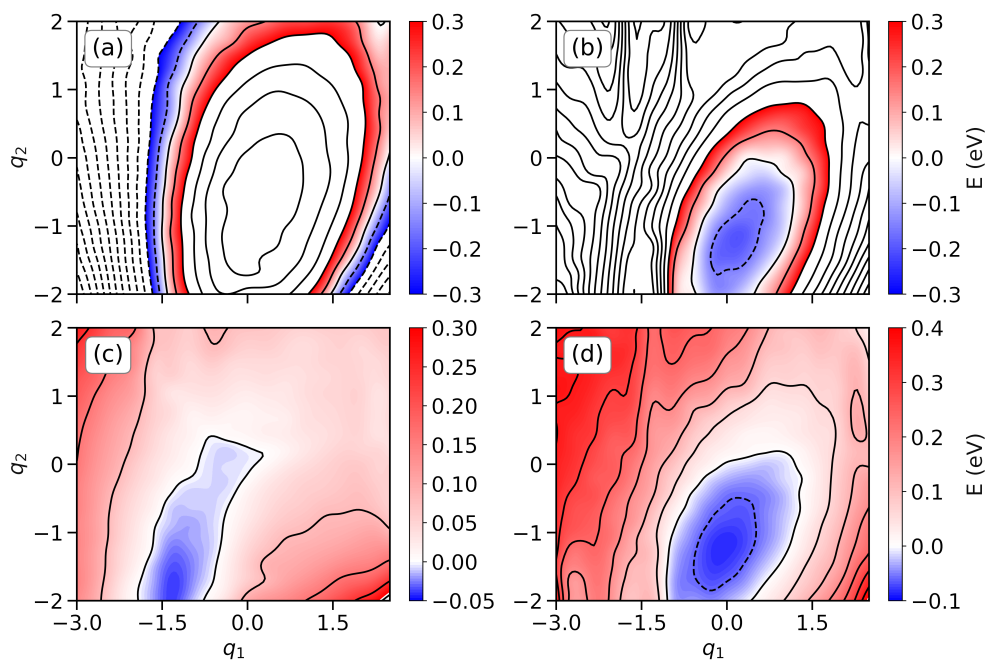


Figure S8. Diabatic potential energy differences and diabatic couplings: (a) $S_2 - S_1$; (b) $S_3 - S_2$; (c) S_2/S_1 diabatic coupling; (d) S_3/S_2 diabatic coupling.

S5 . SHARC POPULATIONS OF BP AND M-BP

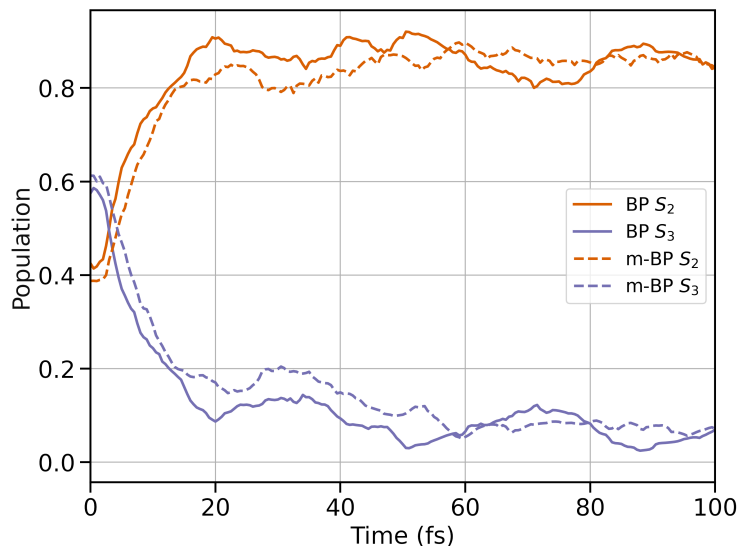


Figure S9. Comparison of the adiabatic SHARC populations of the S_2 and S_3 states of benzophenone (solid lines) and *meta*-methyl benzophenone (dashed lines), within the initial 100 fs.

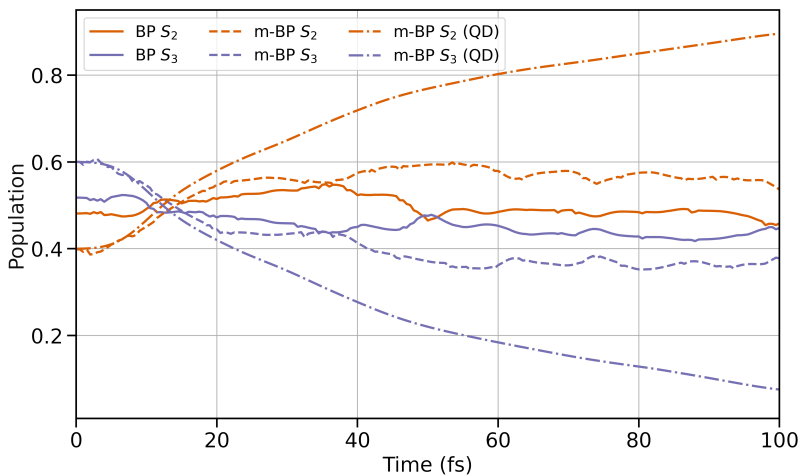


Figure S10. Temporal evolution of diabatic SHARC populations for the S_2 and S_3 states in benzophenone (solid lines) and *meta*-methyl benzophenone (dashed lines), alongside diabatic populations of *meta*-methyl benzophenone derived from QD simulations (dashed-dotted lines).

-
- [1] Takao Itoh. Emission characteristics of benzophenone vapor at low pressure. *J. Phys. Chem.*, 89(19):3949–3951, September 1985.
- [2] Dumitru-Claudiu Sergentu, Rémi Maurice, Remco W A Havenith, Ria Broer, and Daniel Roca-Sanjuán. Computational determination of the dominant triplet population mechanism in photoexcited benzophenone. *Phys. Chem. Chem. Phys.*, 16(46):25393–25403, December 2014.
- [3] Vicenta Sauri, Luis Serrano-Andrés, Abdul Rehaman Moughal Shahi, Laura Gagliardi, Steven Vancoillie, and Kristine Pierloot. Multiconfigurational second-order perturbation theory restricted active space (RASPT2) method for electronic excited states: A benchmark study. *J. Chem. Theory Comput.*, 7(1):153–168, January 2011.
- [4] Per Ake Malmqvist, Kristine Pierloot, Abdul Rehaman Moughal Shahi, Christopher J Cramer, and Laura Gagliardi. The restricted active space followed by second-order perturbation theory method: theory and application to the study of CuO₂ and Cu₂O₂ systems. *J. Chem. Phys.*, 128(20):204109, May 2008.
- [5] Lukas Kurtz, Angelika Hofmann, and Regina de Vivie-Riedle. Ground state normal mode analysis: Linking excited state dynamics and experimental observables. *J. Chem. Phys.*, 114(14):6151–6159, April 2001.